



Numerical model of heat transfer during laser powder bed fusion of 316L stainless steel

Bryce Cox¹ · Milad Ghayoor^{1,2} · Ryan P. Doyle^{1,2} · Somayeh Pasebani^{1,2} · Joshua Gess¹

Received: 4 August 2021 / Accepted: 5 November 2021 / Published online: 16 January 2022
© The Author(s), under exclusive licence to Springer-Verlag London Ltd., part of Springer Nature 2021

Abstract

The laser powder bed fusion (LPBF) process can be used to manufacture parts of unique design that cannot be manufactured using classical methods. The capabilities of LPBF can be expanded upon by introducing metal matrix composites to attain specific property enhancements in the created part, but technical and cost challenges exist that impede the development and advancement of this process. Further understanding of the fundamental thermal and fluid dynamic mechanisms that occur during the LPBF process is required to overcome the challenges and minimize the cost of these advancements. For this study, a numerical model of the LPBF process is created and used to explore relationships between these fundamental mechanisms. A three-dimensional, transient, finite difference numerical heat transfer model is created using MATLAB to predict the temperature and state (powder, liquid, or solid) of 316L stainless steel throughout the LPBF process. The effective thermal conductivity of the metal powder was measured using a laser pulse method for use in the model. Model results are compared to single track samples created with LPBF. The model results for melt pool area show good agreement with the physical samples.

Keywords Laser powder bed fusion · Heat transfer · Heat flow

1 Introduction

Functionally graded alloys (FGAs) designed for a specific performance or function in which a spatial gradation in microstructure and/or composition lends itself to tailored properties that vary with location in the material [1]. Examples of applications of FGAs are their use in heat sinks, biomedical applications, rocket heat shields, heat engine components, and plasma facings for fusion reactors in a nuclear reactor plant [2–4]. For example, FGA heat sinks, with selectively distributed and targeted thermal properties, will allow for conventional cooling mechanisms (i.e. single-phase liquid or air) to more effectively manage non-uniform heating profiles. Conventional heat sinks are designed for isothermal or isoflux heating conditions, which is almost

never the case, while FGAs can eliminate the reliability-robbing internal stresses from coefficient of thermal expansion (CTE) mismatch internal stresses within fragile microelectronics, as much as 6.5 psi, which mandate the use of damping but performance robbing elastomer-based Thermal Interface Material (TIM) attachment pads. A fully functional FGA heat sink will reduce the thermal resistance for any heat sink application by as much as 10–20% as a result of enabling more thermal-friendly TIM attachment options.

FGAs can be created using additive manufacturing technology like laser powder bed fusion (LPBF), but technical and cost challenges exist that prevent selectively adding second phase nanoparticles to a powder bed matrix [1, 5]. A more feasible option is to create a metal matrix composite (MMC) using ball milling and powders mixing prior to melting [6]. However, ball milling has several disadvantages such as change in powder shape and size, cross contamination, and heterogenous distribution of reinforcement particles which cannot create a graded composition within the powder to manufacture FGAs. Furthermore, in order to reduce the time and cost of manufacturing, intermediate and time-consuming stages such as ball milling must be eliminated. Additionally, ball-milling changes the morphology of the

✉ Bryce Cox
coxby@oregonstate.edu

¹ School of Mechanical, Industrial and Manufacturing Engineering, Oregon State University, Corvallis, OR 97330, USA

² Advanced Technology and Manufacturing Institute (ATAMI), Corvallis, OR 97330, USA

powder and reduces flow, packing, and wetting properties leading to higher porosity and cracking in the as-built components. Further understanding of the fundamental thermal and fluid dynamic mechanisms that occur during the LPBF process is required to overcome the challenges and minimize the cost of using LPBF to create FGAs. For this study, a numerical model of the LPBF process is created and used to explore relationships between these fundamental mechanisms that have not yet been discussed in literature.

Many studies have been published that enhance understanding of the LPBF process. Lei et al. [7] used a numerical model of laser welding with power feeding that includes molten pool dynamics, heat transfer, and powder transport to study the impacts of Al powder feeding on the thermodynamics of keyhole type laser welding, including impacts on local high and low temperatures. They reported that increasing laser power created a more stable keyhole, and that higher powder impact velocity led to smaller keyhole entrance size. Gusarov et al. [8] used a combined conduction and radiation thermal model to examine single track laser melting of 316 stainless steel powder on a solid substrate. They used the model to compare results with varying laser speeds and found that scanning speeds over 20 cm/s tended to cause an undesired balling effect in the printed part, due to Plateau-Rayleigh capillary instability. LPBF of Inconel 718 was studied by Lee and Zhang [9] using a powder packing model combined with a heat and fluid flow model to examine the effects of overlapping laser passes on the melt pool shape. They observed a symmetrical pool shape for the first pass, but an asymmetric melt pool shape in the second pass and beyond. This is due to the material not cooling completely between passes and variations in the material properties, since on the second pass, some of the powder has already melted and solidified.

Tran and Lo [10] developed a new volumetric heat source model to represent the laser heat source in LPBF of stainless steel that accounts for the effect of powder size on laser energy penetration. Their work provides insight into process parameters that lead to a stable laser pass and minimizes unwanted balling. Xiao and Zhang [11] created a full fluid dynamics and heat transfer model that they used to study the effects of multiple layers of sintered material below the powder being actively fused. Xiao and Zhang [11] found that an increase in the number of layers below the active layer requires an increase in laser power. Another finding of their study was that an increase in scanning velocity will also require higher laser intensity to achieve sufficient overlap in melting of multiple layers. Papazoglou et al. [12] used a thorough heat transfer model that included raytracing for computing laser power penetration into a stainless steel powder bed to quantify heat losses in the LPBF process from ablation of powder particles. Liao et al. [13] used a model to predict the motion of Al_2O_3 particles during

LPBF, allowing an estimate of the material losses during the process. Using a model for LPBF that accounts for a random particle distribution in the powder bed, Khairallah and Anderson [14] reported that the velocities associated with buoyancy in molten stainless steel were small when compared to velocities driven by surface tension gradient (Marangoni flow). Verhaeghe et al. [15] used an enthalpy based model of LPBF to find that the rate of evaporation of powder particles increases with increasing laser power. While these many studies indicate that a substantial knowledge base exists for the LPBF process, because it is a complex multiphase, multi-physical process further investigation is required. This is particularly true for efforts to advance the LPBF process and associated technology.

This study uses a custom made, transient, numerical heat transfer model to provide additional insights into the LPBF process. This work is part of a multi-year project with the end goal of providing a custom, self-contained software program that can be used to design functionally graded parts to be printed with LPBF. The anticipated final result is a software that takes design criteria as input from the user; then, the software uses the model discussed in this paper, along with flow simulations from future work, to determine where augmenting nanoparticles need to be placed in the powder bed for desired mechanical/thermal performance in the printed part. In order to have a single, packaged software for this design use, a custom code was developed for the simulations to avoid dependence on a separate finite element analysis software. This study also experimentally measures the effective thermal conductivity of the 316L stainless steel powder for use in the model. The knowledge gained here will be implemented in our future work focused on LPBF process of MMC and later on FGAs to understand the effect of thermal and fluid flow mechanisms in distribution of second phase nanoparticles in the 316L matrix.

2 Model development

A three-dimensional, transient, finite difference numerical heat transfer model is created using MATLAB to predict the temperature of 316 stainless steel throughout the LPBF process, and track when the powder transitions to molten liquid or cools to a solid. A uniform mesh (meaning the same grid size, Δx , is used in all three directions x , y , z) was used, with calculations being performed at each node, representing a cubic control volume. Figure 1 shows the node with associated control volume and the coordinate system used.

The energy balance method was used to develop the equations for each node. The volume of each node is assumed to be constant so that a uniform grid can be used. To establish consistent sign notation, heat flux into

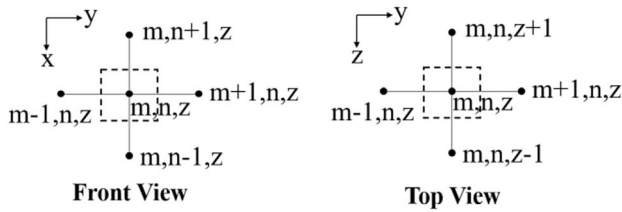


Fig. 1 Front view and top view of an internal node showing the coordinate system

the node will be considered positive. This means that for the development of the equations, heat flux is assumed to be positive, with heat flowing from each neighboring node into the node of interest, nodes $m, n,$ and z in Fig. 1. Equation 1 shows the basic energy balance:

$$\rho c \nabla \frac{\partial T_{m,n,z}}{\partial t} = \sum_{i=1}^6 q''_{nodei \rightarrow m,n,z} \Delta x^2 \tag{1}$$

Looking at the heat flux from node $m - 1, n, z$ to nodes $m, n,$ and z as a representative heat flux term with the positive x direction defined as into the node, and using Fourier’s Law, the result is Eq. 2:

$$q''_{m-1,n,z \rightarrow m,n,z} = -k \frac{\partial T}{\partial x} \tag{2}$$

Using a simple finite difference approximation, this becomes

$$q''_{m-1,n,z \rightarrow m,n,z} = -k \frac{T_2 - T_1}{\Delta x} = -k \frac{T_{m,n,z} - T_{m-1,n,z}}{\Delta x} = k \frac{T_{m-1,n,z} - T_{m,n,z}}{\Delta x} \tag{3}$$

Using a forward difference numerical approximation with a uniform grid, the energy storage term becomes

$$\rho c \nabla \frac{\partial T_{m,n,z}}{\partial t} = \rho c \Delta x^3 \left(\frac{T_{m,n,z}^{P+1} - T_{m,n,z}^P}{\Delta t} \right) \tag{4}$$

Substituting the heat fluxes for temperatures using Eq. 3 for each node neighboring $m, n,$ and $z,$ into Eq. 1 along with the numerical energy storage term from Eq. 4, the overall energy balance becomes

$$\rho c \Delta x^3 \left(\frac{T_{m,n,z}^{P+1} - T_{m,n,z}^P}{\Delta t} \right) = \Delta x^2 \left(\frac{k}{\Delta x} \right) \left(T_{m-1,n,z}^P - T_{m,n,z}^P + T_{m+1,n,z}^P - T_{m,n,z}^P + T_{m,n-1,z}^P - T_{m,n,z}^P + T_{m,n+1,z}^P - T_{m,n,z}^P + T_{m,n,z-1}^P - T_{m,n,z}^P + T_{m,n,z+1}^P - T_{m,n,z}^P \right) \tag{5}$$

Using this energy balance, the temperature for the next time step is calculated using information from the current timestep.

2.1 Boundary conditions

Figure 2 shows the setup of the mesh at the top surface and the heat fluxes included at that surface. The heat fluxes 1, 2, and 3 shown in Fig. 2 are set up in the same way as the node to node heat fluxes for the internal nodes. The laser heat flux is time dependent and represented with multiple models. First, losses are subtracted from the output power reported by the laser hardware. Then, a simplified Gaussian model was used to model the variation of laser power inside the laser diameter where r is the distance from the center of the laser in terms of coordinates y and z [16].

$$q''_L(y, z) = q''_0 \exp\left(\frac{-r^2}{r_0^2}\right) \tag{6}$$

Laser penetration into the powder bed was modeled using a correlation created from the data of Wang et al. [17].

$$q''(x, y, z) = q''_L(y, z) * 0.9909 \exp(-6791x) \tag{7}$$

The net radiative exchange between the powder surface and the surroundings was modeled as shown in Eq. 8.

$$q''_{Rad} = \alpha \sigma T_\infty^4 - \epsilon \sigma T_s^4 \tag{8}$$

The convective flux was modeled as shown in Eq. 9:

$$q''_{Conv} = h(T_\infty - T_s) \tag{9}$$

The powder bed and underlying build plate are assumed to continue beyond the sides and bottom of the mesh. For the thermal conditions at these boundaries, the temperature gradient was calculated at the boundary, and then used to estimate the heat flux into the node from outside the boundary. The temperature gradient in the direction of into the node from the boundary was calculated using a three-point numerical derivative. This is illustrated in Fig. 3 showing the boundary at $y = 0.$

$$q''_B = -k \frac{\partial T}{\partial y} \sim -\frac{k}{2\Delta y} (3T_{m,n,z} - 4T_{m+1,n,z} + T_{m+2,n,z}) \tag{10}$$

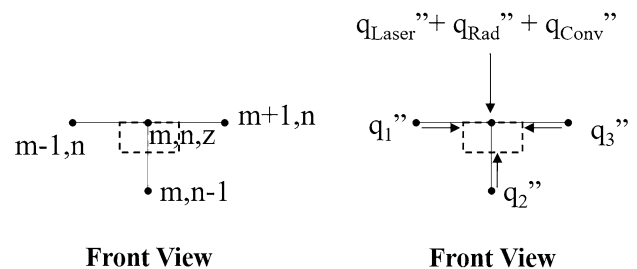


Fig. 2 Nodes near the surface showing surface heat fluxes

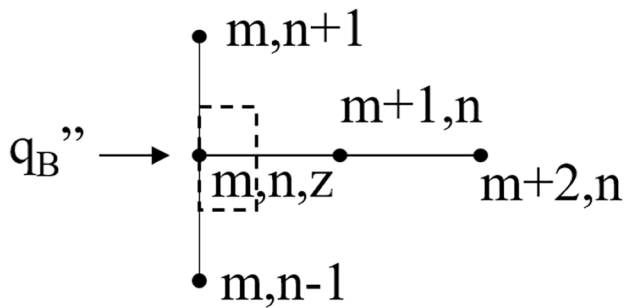


Fig. 3 Side view of a node on the boundary at $y=0$

There are other physical phenomena in the LPBF process that cannot be captured by the proposed conduction-focused heat transfer model in the current form, including evaporative recoil pressure, buoyancy driven flow, Marangoni flow, and other surface tension effects. To account for the impact of these effects, correlations are developed based on the sample measurements used in this study and are empirically applied to the model. The net effect of these interdependent phenomena is driven primarily by the applied laser powers. The laser power-dependent correction factors, cf_1 and cf_2 , are added to Eq. 7, as shown in Eq. 11. The values of cf_1 and cf_2 for various laser power settings are listed in Table 1.

$$q''(x, y, z) = cf_1 * q_L''(y, z) * 0.9909 \exp(-6791x * cf_2) \quad (11)$$

The correction factor cf_1 decreases initially as vaporization near the powder surface reduces the transmission of laser power into the particle bed. This vaporization effect is expected to increase with increasing laser power or reducing the layer thickness, which results in reduced effective laser power and a decrease in cf_1 [7]. There is a transition between 100 and 150 watts of laser power, and the melt pool dynamics becomes less dominated by heat conduction, and instead is dominated by the effect of flow dynamics [12]. Effective laser power increases to account for this flow effect in both the magnitude of laser power, cf_1 , and the laser power penetration into the powder bed, cf_2 .

Table 1 Laser power dependent correction factors

Laser power (W)	cf_1	cf_2
50	0.725	1
100	0.4955	1
150	1	0.8
200	1.09	0.799

2.2 Grid independence

To minimize the dependence of the model results on the grid and timestep size used here, a grid dependence study was performed. The model was run multiple times while decreasing grid size, and the impact on model results was examined. The temperature at three different depths in the powder bed was tracked, and the results compared for the decreasing grid size. Table 2 shows the grid size and the corresponding change in temperature when compared to the previous grid size. For example, the initial grid size used was 2.22×10^{-5} m, since this is the initial run, there are no previous results to compare to. But for the next run, a grid size of 1.82×10^{-5} m was used. When comparing the results using this grid size, to the previous grid size, the temperatures vary by an average of 27.6%, which shows that this change in grid size has a significant impact on results. This temperature variation was calculated by taking the difference in temperature at a given location between the new and previous grid size, then dividing that difference by the temperature at the new grid size. The percentage was calculated for the three locations and then averaged. This process was repeated with decreasing grid size until, when going from a grid size of 8.0×10^{-6} to 5.71×10^{-6} m, the temperature varied by only 0.5%. This indicates that the grid is sufficiently fine to no longer impact the results in a significant way. So the grid size of 8.0×10^{-6} m was used, as reducing the size of the grid beyond this value will not result in substantial changes in simulation results. A similar study was done to examine the impact of the timestep size on these temperature results. The initial timestep used is 1×10^{-6} s. This initial timestep size is used because larger timesteps cause instabilities to arise. A smaller timestep of 5×10^{-7} was used, and the resulting temperatures compared to those from the initial timestep size. The resulting average temperature variation was only 0.41%, indicating that reducing the timestep size will not substantially affect the simulation results. Based on these runs, the grid size and timestep were selected so that continuing to decrease the grid size and/or timestep size will change the temperature results by < 1%. This provides confidence that the timestep and grid size selected have minimal impact on the model results.

Table 2 Grid size and corresponding change in temperature with reduced grid size

Grid size (m)	Temperature variation
$2.22E-05$	-
$1.82E-05$	27.6%
$1.25E-05$	27.1%
$9.52E-06$	23.8%
$8.00E-06$	17.7%
$5.71E-06$	0.5%

Table 3 Properties used in the simulation obtained from literature

Property	Value	Reference
Apparent density of 316L powder	4427.2 kg/m ³	Measured
Tap density of powder	0.6	Trap et al. [18]
Spreading density of powder	4.25 g/cm ³	Measured
Particles size distribution	D10: 18 μm, D50: 30 μm, D90: 49 μm	Measured
Emissivity of 316L powder*	0.6	Gunther et al. [19]
Emissivity of molten 316L	0.28	Fukuyama et al. [20]
Specific heat of 316L powder	0.1097 + (3.174 × 10 ⁻⁵ T) cal/g	[21] [22]
Specific heat of molten 316L	0.184 cal/g	Kim [22]
Density of molten 316L	7.4327 + ((3.9338 × 10 ⁻⁵ T) - (1.8007 × 10 ⁻⁷ T ²)) g/m ³	Kim [22]
Thermal conductivity of molten 316L	124.1 + (3279 × 10 ⁻⁵ T) w/mk	Kim [22]
Convective heat transfer coefficient	10 w/m ² k	Zhang et al. [23]
Laser beam diameter	40 μm	
Laser scanning speed	200 mm/s	

*Number for slightly oxidized 316L powder at elevated temperature

2.3 Material properties

The various material properties used in the simulation are listed in Table 3. The effective thermal conductivity of the powder bed requires special consideration. Depending on the particle size distribution of the metal powder, the shape of the metal particles, and the tap density and spreading density, the effective thermal conductivity of the powder bed can vary significantly. Published values for the thermal conductivity of 316L stainless steel powder vary by 2 orders of magnitude from 0.156 to 39.95 w/m k [14, 24]. In order to accurately represent the 316L stainless steel powder used in the measurements for this study, the thermal conductivity was measured experimentally as explained in the following section.

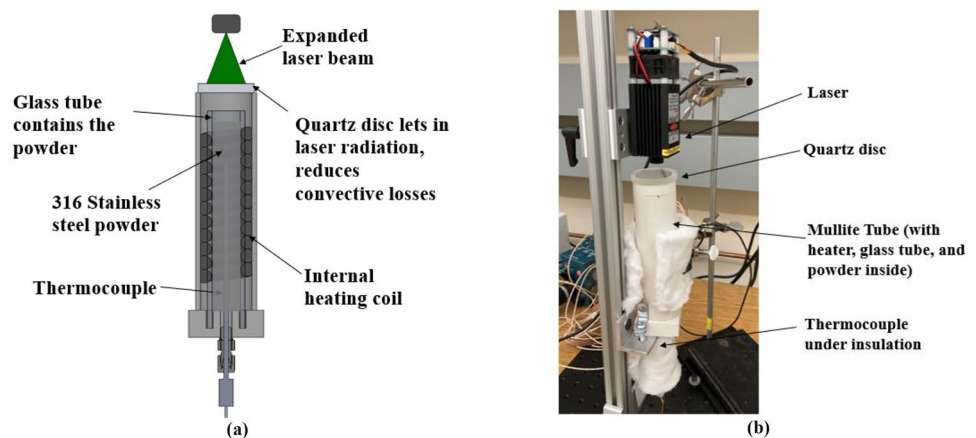
3 Thermal conductivity measurements

The thermal conductivity measurements were taken according to the laser pulse method published by Sih et al. [25]. Figure 4 shows a schematic of the experimental setup and experimental facility, respectively. Gas atomized 316L

stainless steel powder with spherical shape was placed in a glass tube exposed to ambient lab conditions. A type-k thermocouple was located in the powder to measure the powder temperature. The temperature was measured using an NI-9213 thermocouple card using an NI cDAQ-9718 chassis at a sampling frequency of 10 Hz. The accuracy of the thermocouple was ± 2.25 °C. A heating coil was placed over the glass tube for the temperature control. A mullite cylinder was placed on the outside of the heating coil to act as insulation. A quartz disc was placed at the top of the mullite cylinder to allow laser radiation to pass through, but limit air leakage from the cylinder.

For each test, the setup was brought up to temperature by the heating coil while the powder temperature was measured by the thermocouple. The temperature was determined to be constant when it varied by < ±0.3°C for at least 3 min. Once the temperature reached a steady state value, the 15-W laser with 450 nm wavelength was powered on for 4 min and 22 s, applying its radiation to the top of the 316L powder. The temperature rise of the bulk powder was then compared to a solution for a 1-D semi-infinite

Fig. 4 **a** A schematic of the experimental setup to measure thermal conductivity of 31L powder used in this study, and **b** experimental facility while running the measurement



conduction problem [26]. Thermal conductivity was varied using the 1-D solution to find the thermal conductivity that precisely matched the measured temperature variation. Data was taken for temperatures ranging from room temperature up to 700 °C, with the maximum temperature being limited by the maximum operating temperature of the heater. The results of this testing are shown in Fig. 5. The error bars on the plot represent the standard error from the measurements using a student t-distribution with a 95% confidence interval. The measured thermal conductivity values were in agreement with predicted values, as both the thermal conductivity of air and solid stainless steel increased with increasing temperature. A linear regression of the data resulted in the relation for thermal conductivity as a function of temperature, in Celsius, that is shown in Eq. 13. The standard error of the fit for the trendline was 1.423 w/m k.

$$R = \frac{T_2 - T_0}{T_1 - T_0} = \frac{\sqrt{2} \operatorname{ierfc} \left[\frac{L}{2\sqrt{\frac{k}{c_p} t_2}} \right]}{\operatorname{ierfc} \left[\frac{L}{2\sqrt{\frac{k}{c_p} t_1}} \right]} \quad (12)$$

$$k = 0.0167T + 8.5961 \quad (13)$$

4 Materials and methods

To provide model validation, samples were created using ORLAS Creator LPBF machine equipped with a continuous wave Yb: YAG fiber laser (wavelength of 1067 nm) and a stainless-steel build plate. Laser melting was performed in a

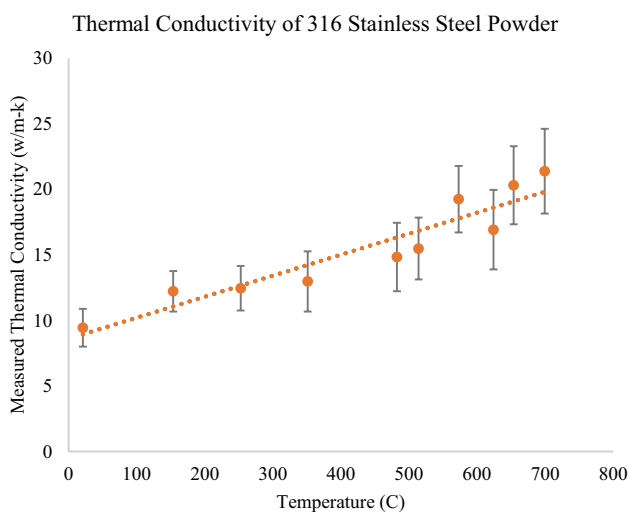


Fig. 5 Thermal conductivity of 316L powder measured experimentally

nitrogen atmosphere, keeping the oxygen level in the build chamber < 100 ppm to minimize oxidation. Each single track was manufactured using a single-layer 316L powder with thickness of 50 μm on a solid stainless steel build plate. Samples were additively manufactured using laser power settings of 50, 100, 150, and 200 W. To maintain a constant layer thickness throughout the whole experiment, a groove with the dimensions of 12 mm in length, 200 μm in width, and 50 μm in depth, representing a typical layer thickness, has been micromachined into the 316L build plate. Then, the 316L powder was spread on top of the groove to fill the groove, and then manually with the aid of a razor blade, a smooth surface on the top of the groove was achieved. Afterward, the laser beam, previously has been aligned with the center of the groove, hit the metal powder and deposited the melt track at the bottom of the groove. Samples were created with the laser powers of 50, 100, 150, and 200 W, and the scan speed of the laser for all samples was 200 mm/s. The deposited single tracks were sectioned along the perpendicular direction to the scanning track. To reveal the melt pool boundaries in optical microscopy, the samples were mounted and polished following the standard metallography procedure and before the examination, were electroetched using a solution of 10 wt% oxalic acid and 90 wt% deionized water, applying 15 V DC for 15 s. Figure 6 shows the samples that were manufactured for comparison to the modeling results. It should be noted that the area to the left of the melt pool on the 100 W sample, in Fig. 6, is a result of the laser alignment process, and is not part of the melt pool examined in this study.

5 Results and discussion

The metric that was used to compare the physical samples to the model results was the cross-sectional area of the melt pool (μm²). Table 4 shows the results for the cross-sectional area measured from the samples and resulting from the model. Figure 7 shows side by side comparisons of the cross sections of the model results and the physical samples. In the figure, the green represents the melt pool, the red is the underlying build plate, and the blue is the powder bed.

As can be seen from the results in Table 4, the model predicts melt pool areas that are very close to the values measured from the experimentally manufactured single tracks. The correction factors discussed earlier can provide some insight about these effects. The factor cf_1 represents the effective laser power that reached the powder bed. This factor initially decreased with increasing laser power. Verhaeghe et al. [15], Gusarov et al. [8], and Papazoglou et al. [12] all discuss how the ablation or vaporization of powder particles results in a decrease of effective laser power, and the rate of vaporization increases with increasing laser power.

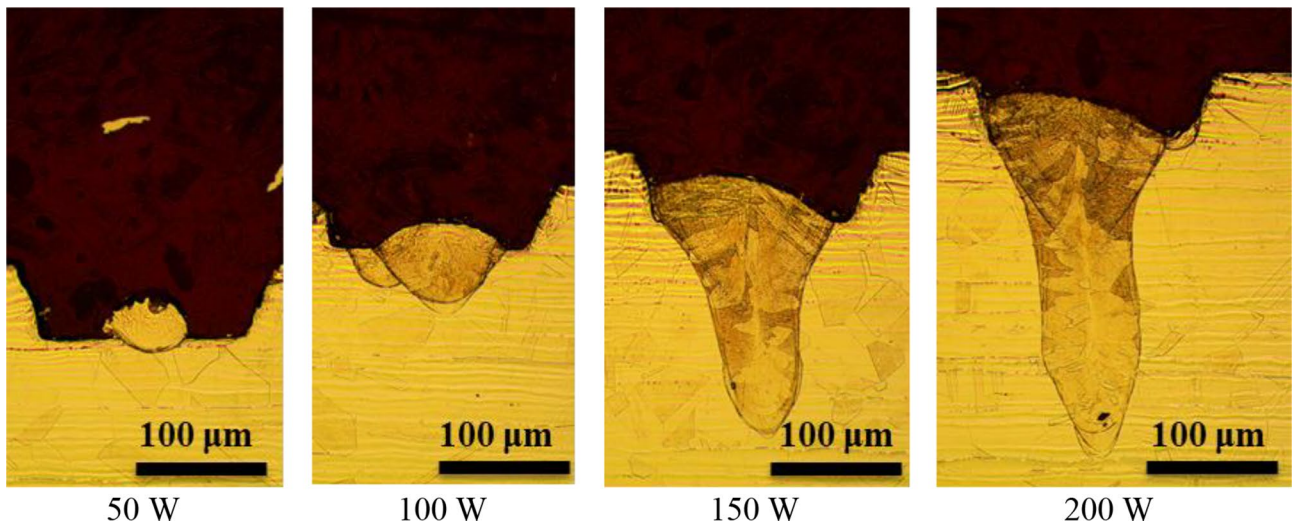


Fig. 6 Optical micrographs of top and cross section views of single track 316L manufactured using LPBF process with powers varying from 50 to 200 W, and scanning speed of 200 mm/s on a build plate

The decrease in the value of cf_1 follows this trend at laser power < 150 W, as increased vaporization losses result in a lower effective laser power. At 150 W and above, there is a reversal, the effective laser power required to match the experimental results increases. If vaporization increases with laser power, as established earlier, then why does the factor cf_1 need to increase to match experimental results? This factor represents effective laser power, which is expected to decrease from this vaporization at higher laser powers. Le and Lo [27] and Papazoglou et al. [12] state that at higher laser powers, fluid dynamic effects become dominant. These effects, including buoyancy-driven motion and Marangoni flow, spread heat into the powder bed through convection, creating a larger melt pool. The conclusion that can then be made from the factor cf_1 is that fluid dynamic effects are significantly more impactful on melt pool size than the reduction in effective laser power associated with vaporization. Vaporization causes a decrease in cf_1 , fluid effects result in an increase in cf_1 . The overall increase in cf_1 shows that fluid effects impact melt pool size more than losses to vaporization. Even though vaporization is reducing the effective laser power that gets to the powder bed, the heat spread by fluid motion effects more than makes up for this reduced effective power at higher laser powers.

Table 4 Comparing cross-sectional area of melt pool in the model and experiment

Laser power (w)	50	100	150	200
Sample area (μm^2)	1790	4285	14,886	21,016
Model area (μm^2)	1784	4288	14,912	21,120
Difference %	0.3%	0.1%	0.2%	0.5%

When comparing the optical micrographs of the LPBF manufactured single tracks to the results from the model, the shapes of melt pools show some similarities in the x -direction, but also some differences in the y -direction. At the lower laser powers, 50 and 100 W, the single track melt pools were much more circular than the results from the model. For the higher laser powers, 150 and 200 W, the shapes show more similarities. In both cases, the melt pool depth is greater than melt pool width. In the experimentally manufactured single tracks, the top of the melt pool was wider than the rest, this is present in the model results, but to a much smaller degree. Marangoni flow is common in molten stainless steel, as a gradient in surface tension is created based on the temperature gradients [28]. The increased width at the top of the experimental results is likely due to Marangoni flow near the surface convecting heat into the adjacent areas, increasing the size of the melt pool.

The temperature at a central location was tracked during the simulation of LPBF for the different laser powers. Figure 8 shows the temperature profiles for the node located at the coordinates of 2×10^{-4} m Y , and 2.4×10^{-5} m Z (near the center of the laser path, at the midplane of the volume modeled) and at a depth of 2.4×10^{-4} m in the X direction into the powder bed.

Only a laser power of 200 watts results in melting at this depth, as the other laser powers do not reach the melting temperature of 1630 K. The phase change can also be seen for the 200 W laser power case in the flat portions of the temperature curve near 0.0095 and 0.013 s. These flat portions are a result of the energy contributing to phase change, rather than sensible heating or cooling. After the phase changes, the sensible heating/cooling resumes.

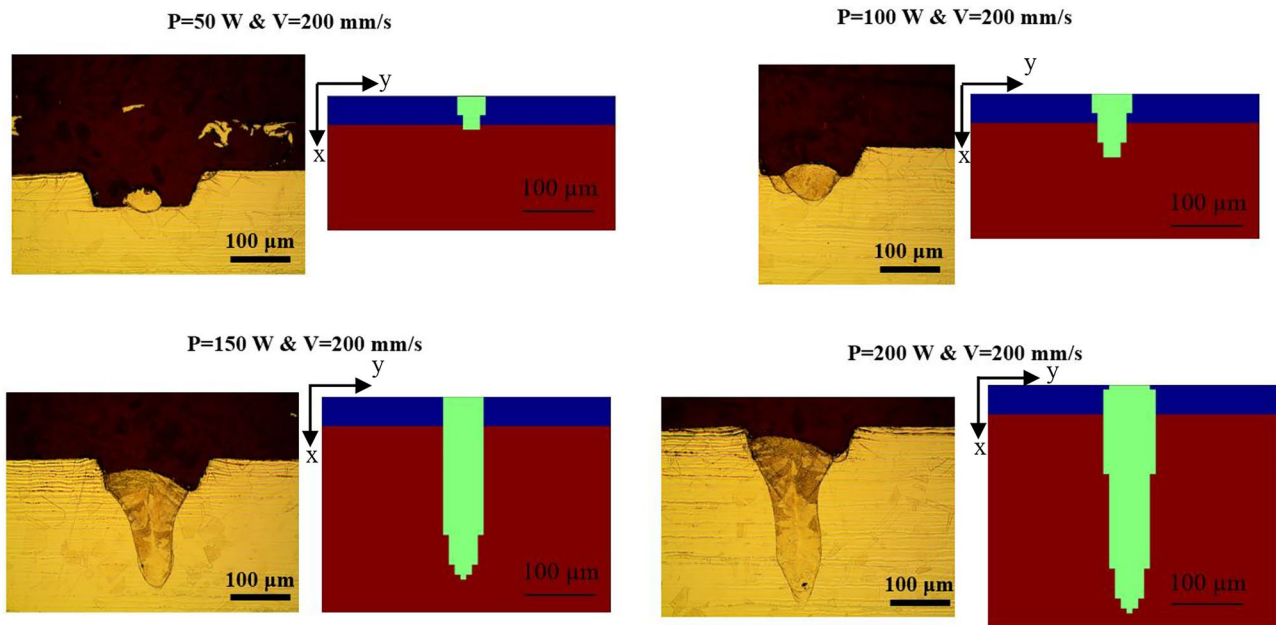


Fig. 7 Side by side comparison of the melt pool cross sections in model and experiments

The relative impact of direct radiation from the laser versus conduction of heat in the powder bed was examined. Based on material properties listed in Table 3 and

grid properties, it is estimated that 3.28×10^{-6} J of energy is required to heat the volume of powder associated with one node from ambient temperature up to melting point

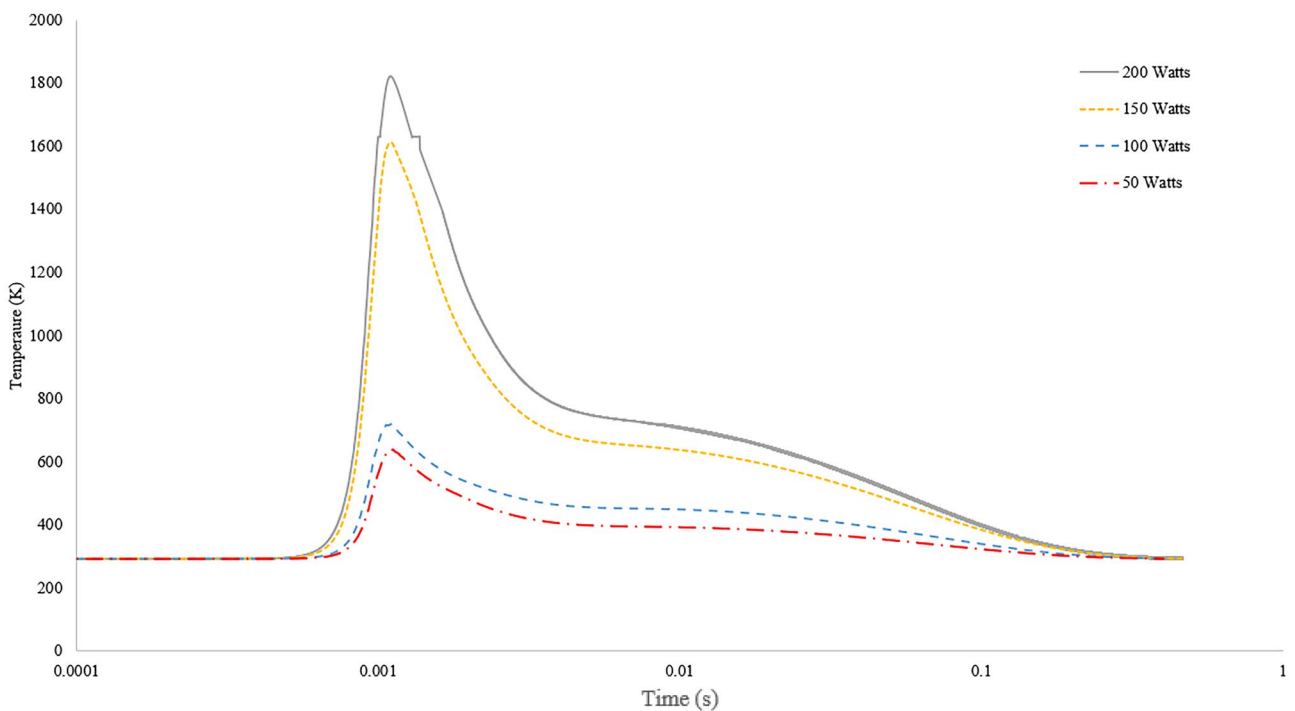
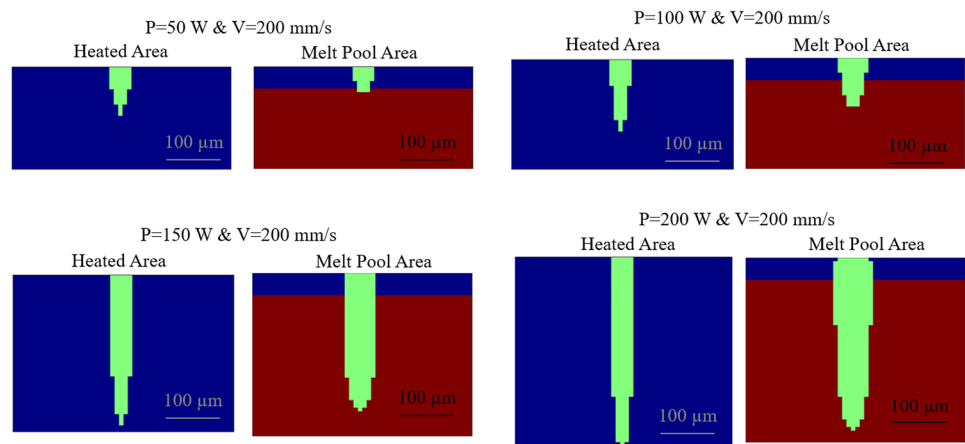


Fig. 8 Temperature during LPBF at the midplane of the model, near the center of the laser path, at a depth of 2.4×10^{-4} into the powder bed

Fig. 9 Comparison of the area that receives sufficient laser power to melt (shown on the left for each laser power) and the area that melts in the simulation (shown on the right)



and melt that volume. From model outputs, how much energy each node receives during the process was calculated. The number of nodes that receive 3.28×10^{-6} J of energy was determined. For this discussion, these nodes that see sufficient energy to potentially melt that node will be referred to as the heated area. This heated area is then compared to the area that actually melts, referred to here as the melt pool. The comparison of these two areas provides insight to how heat is conducted in the powder bed during LPBF. The difference between the heated area and the melt pool model results is due to heat conducting from the nodes that receive laser radiation to adjacent nodes as well as heat losses from convection and radiation from the top level of powder to the surroundings. Figure 9 shows the heated areas and the simulated melt pools for each laser power.

When comparing the heated areas versus the melt pools, near the top of the powder bed, the modeled melt pools tend to be wider than the heated area. This indicates that heat is conducted out laterally, widening the melt pool. Another observation is that the heated area tends to extend further into the powder bed than the melt pool. Although the material at this depth receives sufficient heat to be melted as the laser passes, it does not melt because the heat received by a node is quickly conducted to adjacent nodes before sufficient energy is stored up to melt the material. Table 5 shows the

quantitative difference between the heated area and the melt pool area.

For 50 watts of laser power, the melt pool size is relatively small in comparison to the heated area. At this laser power, the heat has sufficient time to conduct away into the powder bed before enough energy is stored to melt the material, resulting in a smaller melt pool area. As the laser power increases, the heat added becomes more concentrated, and more of the nodes retain sufficient heat to melt before the heat can be conducted away. At 200 watts, the melt pool area is nearly 50% larger than the heated area because at this power, many of the nodes receive much more heat than that required to melt. This excess heat is spread to adjacent nodes, melting them and increasing the melt pool size.

The effect of thermal conductivity on the difference between the heated area and the melt pool size was examined. Figure 10 shows the varying melt pool size for varied thermal conductivities compared to the heated area with a laser power of 150 watts. The quantitative results are listed in Table 6.

Increasing the thermal conductivity increases the melt pool size. This occurs because at 150 watts of laser power, many of the nodes in the heated area receive much more heat than is needed to melt, and with an increased thermal conductivity, more of this heat is conducted to adjacent nodes easily, providing sufficient heat melt additional nodes. Decreasing the thermal conductivity decreases the melt pool area because the heat does not conduct as readily into adjacent nodes, so heat does not spread as readily, and the number of nodes that melt is reduced. Reducing the thermal conductivity causes the shape of the melt pool to more closely resemble the shape of the heated area, which was anticipated as the heated area does not take into account any thermal conduction. As thermal conductivity is reduced, the shape of the pool should trend towards the shape of the heated area.

Table 5 Comparison of area that receives sufficient heat to melt (heated area) and the melt pool area

Laser power (w)	50	100	150	200
Heated area (μm^2)	2880	4160	10,752	14,208
Modeled melt pool area (μm^2)	1784	4288	14,912	21,120
Difference %	62%	103%	139%	148%

Fig. 10 Effect of thermal conductivity on melt pool area

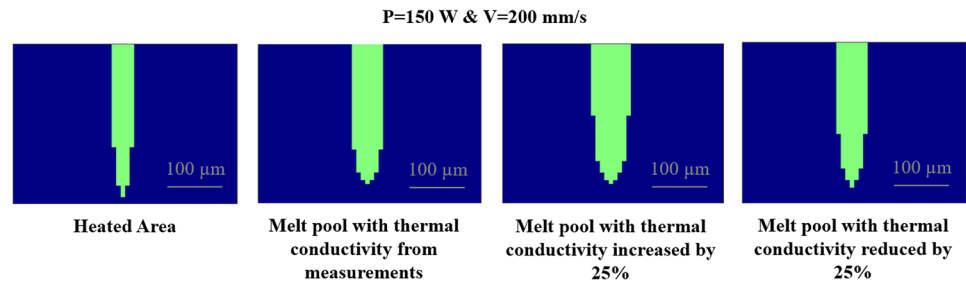


Table 6 Comparison of area that receives sufficient heat to melt (heated area) and the melt pool area for varying thermal conductivity

Thermal conductivity	Increased 25%	As measured	Reduced 25%
Heated area (μm^2)	10,752	10,752	10,752
Modeled melt pool area (μm^2)	17,728	14,912	14,336
Difference %	165%	139%	133%

6 Conclusions and future work

A transient, 3-dimensional, numerical heat transfer model was developed to model the melt pool shape and thermal conductivity of 316L stainless steel powder during LPBF process. The model was validated by comparing the melt pool area predicted by the model to cross sections of experimentally manufactured single tracks. The model results showed good agreement with the observed melt pool. From comparisons of model performance to experimental results, it was concluded that fluid dynamic effects at higher laser powers (> 100 W) had a significantly larger effect on melt pool size than the reduction in the effective laser power associated with powder vaporization. The impact of conduction on the size of the melt pool was examined by comparison of the area of the applied laser power to the melt pool area. Simulations were run with varying thermal conductivity and found that increasing the thermal conductivity increases the melt pool area. The effective thermal conductivity of the 316L stainless steel powder was measured experimentally at multiple temperatures. The slope of the thermal conductivity with respect to temperature and the magnitude of the thermal conductivity fall within expected values. An equation correlating thermal conductivity to temperature is provided.

The major limitation of this custom simulation tool is that it does not account for fluid flow. As discussed above, the motion of the fluid has significant impact on the shape and size of the melt pool. In order to design functionally graded materials created with LPBF, the fluid flow path must be known to relate the initial location of augmenting nanoparticles in the powder bed with the final location of the particles in the built part. To achieve this, continuing work will be done to include fluid flow effects in this custom model including buoyancy and Marangoni driven flows, which will

be used to predict fluid motion and flow paths during the LPBF process. This model will then be packaged with custom design software for use in designing FGAs.

Abbreviations α : absorptivity; ϵ : emissivity; ∇ : volume; ρ : density; σ : Stephen Boltzman; c : specific heat; cf : correction factor; h : convective heat transfer coefficient.; k : thermal conductivity; P : timestep; q'' : heat flux; r : radius; T : temperature; t : time; V : velocity; Δx : grid size

Acknowledgements The authors thank the ATAMI facility staff and director.

Funding National Science Foundation (NSF) Advanced Manufacturing Program (award number: 1856412).

Availability of data and material The datasets generated during and/or analyzed during the current study are available from the corresponding author on reasonable request.

Code availability The software used in this study was Matlab R2020b, which is commercially available.

Declarations

Conflict of interest The authors declare no competing interests.

References

- Bhavar V, Kattire P, Thakare S, Patil S, Singh RK (2017) A review on functionally gradient materials (FGMs) and their applications. IOP Conference Series. Mater Sci Eng 229(1):12021
- You J-H, Brendel A, Nawka S, Schubert T, Kieback B (2013) Thermal and mechanical properties of infiltrated W/CuCrZr composite materials for functionally graded heat sink application. J Nucl Mater 438(1–3):1–6
- Sola A, Bellucci D, Cannilo V (2016) Functionally graded materials for orthopedic applications - an update on design and manufacturing. Biotechnol Adv 34(5):504–531

4. Beal VE, Erasenthiran P, Ahrens CH, Dickens P (2007) Evaluating the use of functionally graded materials inserts produced by selective laser melting on the injection moulding of plastics parts. *Proceedings of the Institution of Mechanical Engineers, Part B: J Eng Manuf* 221(6):945–954
5. Sing SW, An J, Yeong WY, Wiria FE (2015) Laser and electron-beam powder-bed additive manufacturing of metallic implants: a review on processes, materials and designs. *Orthopaedic Research* 34:369–385
6. Ghayoor M, Lee K, He Y, Chang CH, Paul BK, Pasebani S (2020) Selective laser melting of austenitic oxide dispersion strengthened steel: Processing, microstructural evolution and strengthening mechanisms. *Mater Sci Eng* 788:139532
7. Lei Z, Wu S, Li P, Li B, Lu N, Hu X (2019) Numerical study of thermal fluid dynamics in laser welding of Al alloy with powder feeding. *Appl Therm Eng* 151:394–405
8. Gusarov AV, Yadroitsev I, Bertrand P, Smurov I (2009) Model of radiation and heat transfer in laser-powder interaction zone at selective laser melting. *J Heat Transfer* 131(7):072101
9. Lee YS, Zhang W (2016) Modeling of heat transfer, fluid flow and solidification microstructure of nickel-base superalloy fabricated by laser powder bed fusion. *Addit Manuf* 12:178–188
10. Tran HC, Lo YL (2018) Heat transfer simulations of selective laser melting process based on volumetric heat source with powder size consideration. *J Mater Process Technol* 255:411–425
11. Xiao B, Zhang Y (2008) Numerical simulation of direct metal laser sintering of single-component powder on top of sintered layers. *J Manuf Sci Eng* 130(4)
12. Papazoglou E, Karkalos N, Markopoulos A (2020) A comprehensive study on thermal modeling of LPBF process under conduction mode using FEM. *Int J Adv Manuf Technol* 111(9–10):2939–2955
13. Liao H, Zhu J, Chang S, Xue G, Zhu H, Chen B (2020) Al₂O₃ loss prediction model of selective laser melting Al₂O₃–Al composite. *Ceram Int* 46(9):13414–13423
14. Khairallah SA, Anderson A (2014) Mesoscopic simulation model of selective laser melting of stainless steel powder. *J Mater Process Technol* 214(11):2627–2636
15. Verhaeghe F, Craeghs T, Heulens J, Pandelaers L (2009) A pragmatic model for selective laser melting with evaporation. *Acta Mater* 57(20):6006–6012
16. Crafer RC, Oakley PJ (1993) *Laser processing in manufacturing*. 1st ed., Chapman & Hall
17. Wang X, Laoui T, Bonse J, Kruth J, Lauwers B, Froyen L (2002) Direct selective laser sintering of hard metal powders: experimental study and simulation. *Int J Adv Manuf Technol* 19(5):351–357
18. Trapp J, Rubenchik A, Guss G, Matthews M et al (2017) In situ absorptivity measurements of metallic powders during laser powder-bed fusion additive manufacturing. *Appl Mater Today* 9:341–349
19. Gunther M, Susanna N, Simon J, Christiane M, Kai H (2020) Experimental determination of the emissivity of powder layers and bulk material in laser powder bed fusion using infrared thermography and thermocouples. *Metals (Basel)* 10(1546):1546
20. Fukuyama H, Higashi H, Yamano H (2019) Thermophysical properties of molten stainless steel containing 5 mass % B4C. *Nucl Technol* 205(9):1154–1163
21. Klar E, Samal PK (2007) *Powder metallurgy stainless steels; processing, microstructures, and properties*. SciTech Book News 31(4)
22. Kim C (1975) *Thermophysical properties of stainless steels* Argonne National Laboratory, Lemont, IL, United States. Technical Report ANL-75-55
23. Zhang T, Li H, Liu S, Shen S, Xie H, Shi W, Zhang G, Shen B, Chen L, Xiao B, Wei M (2018) Evolution of molten pool during selective laser melting of Ti-6Al-4V. *J Phys D Appl Phys* 52(5):55302
24. Rombouts M, Froyen L, Gusarov AV, Bentefour EH, Glorieux C (2004) Photopyroelectric measurement of thermal conductivity of metallic powders. *J Appl Phys* 97(2):024905–024905–9
25. Sih SS, Barlow JW (2004) The prediction of the emissivity and thermal conductivity of powder beds. *Part Sci Technol* 22(4):427–440
26. Sih SS, Barlow JW (1993) Measurement of the thermal conductivity of powders by two different methods. *International Solid Freeform Fabrication Symposium* 42:370–373
27. Le T, Lo Y (2019) Effects of sulfur concentration and Marangoni convection on melt-pool formation in transition mode of selective laser melting process. *Mater Des* 179:107866
28. Yin H, Emi T (2003) Marangoni flow at the gas/melt interface of steel. *Metall Mater Trans B Process Metall Mater Process Sci* 34(5):483–493

Publisher's Note Springer Nature remains neutral with regard to jurisdictional claims in published maps and institutional affiliations.